Ionics (2020) 26:3815–3821
https://doi.org/10.1007/s11581-020-03503-x

ORIGINAL PAPER

Enhancing the interface stability of $Li_{1.3}Al_{0.3}Ti_{1.7}(PO_4)_3$ and lithium metal by amorphous $Li_{1.5}Al_{0.5}Ge_{1.5}(PO_4)_3$ modification

Lianchuan Li[1] · Ziqi Zhang[1] · Linshan Luo[1] · Run You[1] · Jinlong Jiao[1] · Wei Huang[1] · Jianyuan Wang[1] · Cheng Li[1] · Xiang Han[1,2] · Songyan Chen[1]

Received: 6 January 2020 / Revised: 12 February 2020 / Accepted: 15 February 2020 / Published online: 16 May 2020

Abstract

$Li_{1.3}Al_{0.3}Ti_{1.7}(PO_4)_3$ (LATP) has become the focus of research because of its high ionic conductivity, high oxidation voltage, and low air sensitivity. However, Ti^{4+} is easily reduced by Li metal. In this paper, amorphous $Li_{1.5}Al_{0.5}Ge_{1.5}(PO_4)_3$ (a-LAGP) is introduced as an interface modification layer, because LAGP has the small electrochemical potential difference and Ge^{4+} is more difficult to be reduced by Li. Radio frequency sputtering (RF sputtering) is adopted to modify the a-LAGP thickness less than 100 nm. Compared with crystalline LAGP layer, a-LAGP has a better effect on improving the interface stability of LATP and Li. With the a-LAGP film, the Li/a-LAGP/LATP/a-LAGP/Li symmetrical cell is still stable after 100 cycles with the over potential changing from 1 V to 3 V. The probable mechanism of the good stability between a-LAGP and Li are discussed.

Keywords All-solid-state lithium battery · $Li_{1.3}Al_{0.3}Ti_{1.7}(PO_4)_3$ · $Li_{1.5}Al_{0.5}Ge_{1.5}(PO_4)_3$ protective layer · Stability against lithium · Radio frequency sputtering

Introduction

With the increasing demand for energy storage devices, traditional liquid lithium-ion batteries have been unable to meet the demand due to their low safety and energy density. Meanwhile, all-solid-state metallic lithium batteries have attracted more and more attention [1]. The lithium metal has a higher theoretical specific capacity of 3800 mAh g^{-1} compared with graphitic anode (372 mAh g^{-1}) [2]. Due to the growth of lithium dendrites, Li cannot be used as anode in traditional liquid lithium-ion batteries [3], while the solid electrolyte in solid-state batteries can well inhibit the growth of lithium dendrites [4]. Therefore, all-solid-state lithium batteries can use lithium metal as anode, which enables all-solid-state batteries have higher theoretical specific capacity, higher operating voltage, and more safety than liquid lithium batteries [5].

By now, many solid state electrolytes have been studied, such as oxide solid electrolytes NASICON (e.g., $Li_{1.3}Al_{0.3}Ti_{1.7}(PO_4)_3$ [6], $Li_{1.5}Al_{0.5}Ge_{1.5}(PO_4)_3$ [7]), perovskite (e.g., $Li_xLa_{2/3-x/3}TiO_3$ [8]) and garnet type $Li_7La_3Zr_2O_{12}$ (LLZO [9]), sulfide solid electrolyte (e.g., $Li_7P_3S_{11}$ [10–12]), and Polymer electrolyte [5]. LATP has a relatively high ionic conductivity (7×10^{-4} S cm^{-1}) [4], and it is stable in air [13]. In addition, LATP is convenient for commercialization as the precursors are cheap and preparation process is simple [5]. In summary, LATP is a good choice for solid state electrolyte. However, the contact between LATP and lithium anode will cause Ti^{4+} to be reduced to Ti^{3+} by lithium metal continuously, resulting in the failure of cycling performance [14]. In order to stabilize the interface between LATP and lithium anode, a suitable interface layer should be inserted. As a solid state electrolyte, LLZO has a low reduction potential and has a relative stable contact with lithium metal. However, the wettability between LLZO and lithium is poor, so another modification layer is necessary to optimize the interface between LLZO and lithium anode [15]. West et al. used LiPON to modify the interface [2], but LiPON

✉ Xiang Han
hanxiang@stu.xmu.edu.cn

✉ Songyan Chen
sychen@xmu.edu.cn

[1] Department of Physics, Jiujiang Research Institute, and Collaborative Innovation Center for Optoelectronic Semiconductors and Efficient Devices, Xiamen University, Fujian 361005, People's Republic of China

[2] College of Materials Science and Engineering, Nanjing Forestry University, Nanjing 210037, China

is unstable in the air and is not the best choice for the modification layer. Kotobuki et al. proposed using TiO_2 to modify solid electrolyte [16]. However, there is a big difference between the electrochemical window of LATP and metal oxides such as TiO_2 and Al_2O_3, and their combination will produce a space charge layer, which will hinder the transport of lithium ions [17]. LAGP has the same NASICON structure as LATP, and their electrochemical window are similar [14]. Moreover, the ionic conductivity of LAGP is almost the same with LATP and Ge^{4+} in LAGP is more stable than Ti^{4+} [13], especially at low redox potential. As a consequence, LAGP is a more suitable modification layer between LATP and lithium anode.

Sandwich structure a-LAGP/LATP/a-LAGP solid electrolyte by RF sputtering was prepared, and Li/a-LAGP/LATP/a-LAGP/Li symmetrical cell was assembled. Due to the use of RF sputtering, the thickness of the a-LAGP modified layer can be precisely control, in order that the influence of a-LAGP on the interface impedance can be minimized. Compared with Li/LATP/Li symmetrical cell, Li/a-LAGP/LATP/a-LAGP/Li symmetrical cell has better galvanostatic cycle stability. Then, the symmetrical cell with annealed LAGP/LATP/LAGP electrolyte has been test by galvanostatic cycle, and its cycle stability is not as good as that of the unannealed symmetrical cell. After 50 h of galvanostatic cycling with 0.01 mA cm^{-1} of current density, the over potential of symmetrical cell without a-LAGP increased from 1 to 5 V, and that of symmetrical cell with a-LAGP only changed from 1 to 2.5 V.

Experimentals

Preparation of LATP powders and pellets

According to the stoichiometric ratio of $Li_{1.3}Al_{0.3}Ti_{1.7}(PO_4)_3$, Li_2CO_3, Al_2O_3, TiO_2, and $NH_4H_2PO_4$, precursors were put into an agate mortar, in which Li_2CO_3 was 10 wt% more to offset the loss of lithium in the grinding and sintering processes [18]. The powders were ground for 1 h, and then loaded into a die for pressing. The pressure of 500 MPa was applied to the die by the hydraulic press, and the pressure was kept for 5 min. The compacted sheets were put into corundum crucible and heated to 500 °C at a rate of 2 °C min^{-1} in a tubular furnace. After holding for 6 h, the samples were cooled naturally in the furnace. The expanded sample was crushed, pressed again, and put into the tubular furnace. The temperature rose to 700 °C and hold for 4 h. After that, the sintered samples were grinded, pressed, and sintered for the third time. During the third time, the compression of the sheet shall be carried out in sections, and each increase of 20 MPa pressure shall be stopped for a while to prevent the fragmentation of the sheet body. The last sintering temperature was 900 °C, holding for 6 h. Finally, the pure LATP sheet was obtained with the diameter of 12 mm and the thickness is 1 mm.

Preparation of a-LAGP film

LAGP powder ($Li_{1.5}Al_{0.5}Ge_{1.5}(PO_4)_3$) with 500 nm particle size was supplied from Hefei Kejing Materials Technology Co., Ltd. The prepared LAGP powder was poured into a Cu-disk holder with the diameter of 60 mm, which has a trench of 3 mm depth, and then pressed tightly with a flat stainless steel by hydraulic press [19]. Then, the prepared LAGP target and LATP sheet are put into the sputtering cavity. After the vacuum degree pumped to 1×10^{-4} Pa, magnetron sputtering was carried out in nitrogen atmosphere. The sputtering power was 100 W, the pre-sputtering time was 3 min, and the sputtering time was 30 min. Finally, 100 nm a-LAGP films were deposited on LATP pellets. Moving the sputtered electrolyte tablets into the glove box immediately can avoid the influence of air, so that a-LAGP film has a high and stable ionic conductivity.

Characterization

The crystal structure and purity of LATP pellets and LAGP films were measured by X-ray diffraction (XRD, Rigaku IV, Nippon Science Corporation). The ionic conductivity of LATP was measured by electrochemical impedance spectroscopy (EIS) at the electrochemical workstation (CHI604E, Shanghai Chenhua Instrument Co. Ltd.). The surface morphology of LATP and LAGP was measured by scanning electron microscopy (SEM, Sigma-H, Carl Zeiss Germany) and transmission electron microscope (TEM, Philips Tecnai F30). The determination of molecular structure of LATP and LAGP and the phase analysis before and after the cycle are measured by Fourier infrared spectroscopy (FTIR, NOCOLET380, Thermo Electron Corporation) and Raman spectroscopy (WITECλ = 488 nm).

Electrochemical test

In glove box, the symmetrical cells were assembled with a-LAGP/LATP/a-LAGP electrolytes, lithium anodes, and coin-cell (CR2025). The situation of charging/discharging of symmetrical batteries is given by galvanostatic cycle experiment of landian system (LAND, Wuhan Blue Electric Electronics Co. Ltd.) with a current density of 0.01 mA cm^{-2}, and the charge time of each cycle was 1 h.

Results and discussion

The prepared LATP powders were characterized by XRD, the obtained diffraction pattern is in well consistent with the

standard spectra of LATP, and the peaks were sharp, indicating that the prepared LATP powders have pure phase (Fig. 1a). The XRD patterns of quartz substrate, a-LAGP, and annealed LAGP (900 °C) were tested (Fig. 1b); the pristine quartz shows a blunt peak in the XRD pattern with an angle about 21 degrees. By sputtering an amorphous film of LAGP, the strength of the peak is weakened. After annealing, the peak of LAGP appeared in the curve (below is the standard pattern of LAGP). Because the LAGP film is only 100 nm, it can only be characterized by grazing incidence mode, which leads the peak of LAGP looks weak. Copper blocking electrodes were sputtered on both sides of LATP, a-LAGP/LATP/a-LAGP, and annealed LAGP/LATP/LAGP before EIS test. According to the curve in Fig. 1c and formula

$$\sigma = \frac{L}{RS} \tag{1}$$

where σ is the ionic conductivity, L is the thickness of the sample, R is the total resistance, its value is determined by the abscissa of the inflection point of the curve in Fig. 1c, and S is the surface area of the sample. The calculated ionic conductivity of LATP is 2×10^{-4} S cm^{-1}. The ionic conductivities of a-LAGP/LATP/a-LAGP and annealed LAGP/LATP/LAGP were calculated, respectively. Compared with polycrystalline LAGP, the ionic conductivity of a-LAGP must be lower because there is no ordered Li ion transport channels. The ionic conductivity of LAGP is slightly lower than that of LATP, so the existence of a-LAGP film will lead to the decrease of the total ionic conductivity. However, the influence of sputtered a-LAGP film on the ion conductivity is limited because it is only 100 nm. If the thickness of a-LAGP film is reduced, this effect can be ignored. At the same time, the existence of a-LAGP film is helpful for the fit of LATP and lithium, which reduces the interface impedance and the total impedance of symmetrical cells.

The a-LAGP coating layer morphologies of LATP were characterized by SEM and TEM. In Fig. 2a, LATP shows a typical ceramic surface filled with grains and grain boundaries. The grain size of LATP is relatively large, which is about 5 μm. It can be found that there is a very close contact between the grains. The coating of sputtered a-LAGP on LATP is compact and continuous (Fig. 2b). After annealing, the coverage of LATP by LAGP is still continuous, but appears sharp patterns, implying the crystalline process of LAGP (Fig. 2c). The cross section of a-LAGP/LATP and annealed LAGP/LATP were clearly displayed in high resolution TEM (Fig. 2d and e). From the comparison of the two images, the a-LAGP shows amorphous and uniform coating nature, while annealed LAGP exhibits the existence of some nano crystals. A LATP crystalline grain covered by a-LAGP was caught and analyzed by EDS (Fig. 2f), and Al, Ti, P, O, and Ge all have clear distribution, in which the distribution of Ge shows obviously different morphology. At the edge of the crystalline grain, the brightness of Ge is obviously brighter than that of the middle part, while the brightness of other elements is darker at the edge, demonstrating the LATP is coated by a-LAGP layer.

The samples of LATP, LAGP, annealed LAGP/LATP, and GeO_2 were tested by FTIR (Fig. 3). We found that the peak of LAGP/LATP is the superposition of LATP and LAGP. For LAGP, the peaks at 3419 cm^{-1} are consistent with that at GeO_2. For LAGP/LATP, the above peak in the LAGP are retained, and the LATP curve is also complete, which shows that the double-layer structure of LAGP/LATP prepared by sputtering and annealing is effective and complete.

Li/LATP/Li, Li/a-LAGP/LATP/a-LAGP/Li, and annealed Li/LAGP/LATP/LAGP/Li symmetrical cells were assembled. Galvanostatic cycling was carried out for the symmetrical cells, the charge time of each cycle was 1 h, and the current density was 0.01 mA cm^{-2}. We found that the curve of symmetrical cell is obviously smooth by the modification of a-LAGP (Fig. 4a). The cell with annealed Li/LAGP/LATP/LAGP/Li is not as that with the Li/a-LAGP/LATP/a-LAGP/Li. For Li/LATP/Li, Li/LAGP/LATP/LAGP/Li, and Li/a-LAGP/LATP/a-LAGP/Li, the over potential increment per mAh is 8 V mAh^{-1}, 2.7 V mAh^{-1}, and 1.6 V mAh^{-1} respectively. This proves that the coating of a-LAGP can alleviate the overpotential growth of symmetrical cells during the cycling life. Enlarging the x axis, the curves of the Li/LATP/Li symmetrical cells are obviously different from others (Fig. 4b). For Li/LATP/Li cells, a small overpotential peak can be

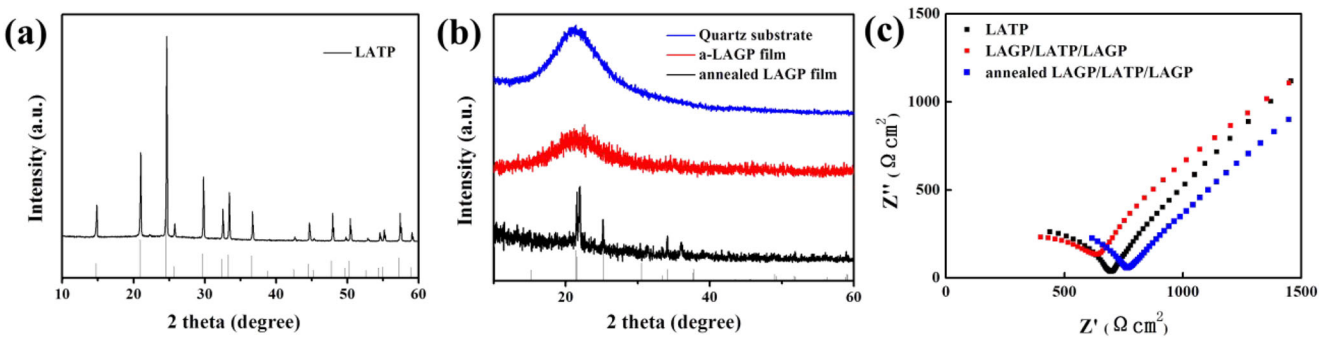

Fig. 1 **a** The XRD pattern of LATP powders. **b** The XRD pattern of quartz substrate, a-LAGP film, and annealed LAGP film on the quartz substrate. **c** EIS of LATP, a-LAGP/LATP/a-LAGP, and annealed LAGP/LATP/LAGP (the AC frequency range is 0.01 to 10^5 Hz)

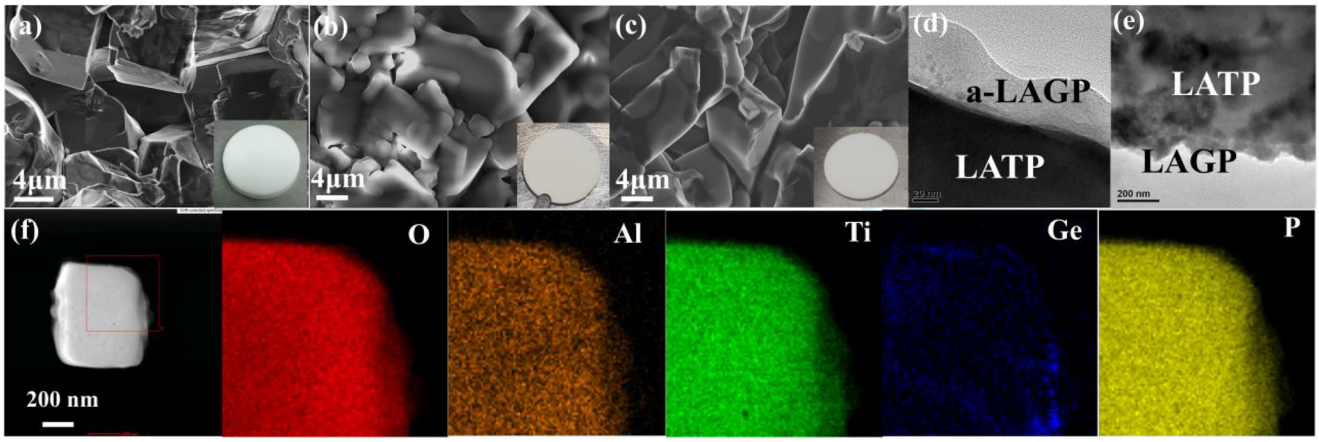

Fig. 2 SEM images. **a** Pristine LATP. **b** Top view of a-LAGP/LATP. **c** Annealed LAGP/LATP. TEM images. **d** Cross section of a-LAGP/LATP. **e** Cross section of annealed LAGP/LATP. **f** elemental analysis of a-LAGP/LATP

seen at the beginning of each cycle. According to the work by Chen et al. [20], this small peak is caused by the formation of lithium dendrites. However, no similar small peak can be seen in the curve of the sample covered with a-LAGP, which indicates that the existence of a-LAGP limits the growth of lithium dendrites.

Li/LATP/Li, Li/a-LAGP/LATP/a-LAGP/Li, and Li/LAGP/LATP/LAGP/Li symmetrical cells were tested with different cycles of galvanostatic cycling, then the symmetrical cells were disassembled and the electrolytes were characterized by SEM (Fig. 5). It can be seen from SEM that with the increase of the number of cycles, the electrolyte surface of Li/LATP/Li symmetrical cell has obvious cracks, the LATP grains fractured into small and irregular particles. The particle fracture may cause by the stress during Li inserted/reacted with LATP, which subsequently induces the failure of mechanical contact or Li pathway between Li and LATP. By contrast, the electrolyte surface of Li/a-LAGP/LATP/a-LAGP/Li shows almost the same morphology after different cycles, implying the stable interface between Li and LATP. The Li/LAGP/LATP/LAGP/Li symmetrical cell has a relatively consistent morphology.

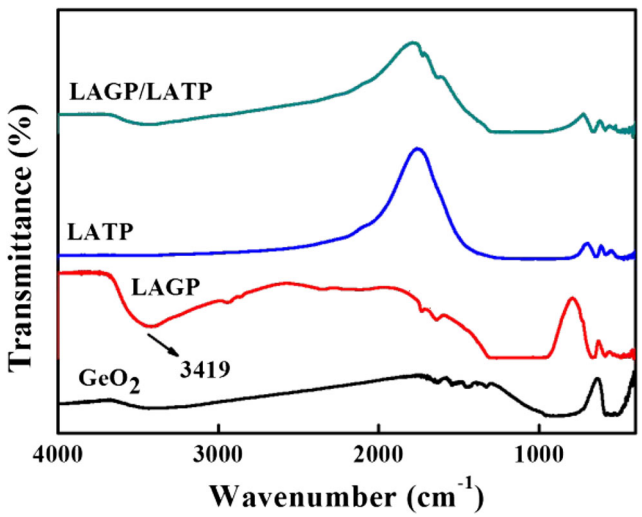

Fig. 3 FTIR spectra. **a** LATP, LAGP, and LATP/LAGP samples. **b** Li_2CO_3, Al_2O_3, TiO_2, $NH_4H_2PO_4$, and GeO_2 precursors

The solid electrolytes after 20 cycles and pristine electrolytes were tested by Raman spectroscopy. For a single LATP pellet, clear characteristic peaks can be seen before the cycle (Fig. 6), which are consistent with the LATP peaks reported in other literature [21]. The bands in the ranges of 860–1130 cm^{-1} and 400–680 cm^{-1} are attributed to the stretching and bending vibrations of the P-O bonds, respectively [22]. The bands present in the lower region are caused by the transitional vibrations of Ti^{4+}, PO_4^{3-} ions, and the librations of PO_4^{3-} [23]. There are three obvious characteristic peaks (969.5 cm^{-1}, 989.1 cm^{-1}, 1007.3 cm^{-1}) near 1000 cm^{-1} [24], and at 20 cycles, the intensity of the peak decreases. With the increase of the cycle number, it can be seen that the three peaks evolve into one peak, implying the structure collapse of LATP. In the paper of Dashjav et.al [21], we know that with the substitution of Li and Al for Ti, the spectral peaks of $Li_{1+x}Al_xTi_{2-x}(PO_4)_3$ gradually widens. The most likely reaction in the symmetrical cell cycle is the reduction of Ti^{4+}, so the peak broadening in Fig. 6 and the situation shown in the paper are mutually confirmed.

For the electrolyte pellet sputtered with a-LAGP and annealed LAGP, an obvious peak can be seen at 782 cm^{-1}, which is the unique peak of LAGP. With the increase of the cycle number, the overall morphology of the peak changed little, which confirms the protection of LAGP to the electrolyte pellet. The peak of 782 cm^{-1} is related to the vibration mode of O-Ge-O [25–28]. In a-LAGP/LATP, the intensity of this peak is very strong, but after annealing, its intensity is weakened a lot. On the contrary, the intensity of the rest peaks in the spectrum is enhanced. This shows that the annealing results in the change of Ge-O bond, which makes the peaks of annealed sample similar to those of Li/LATP/Li after cycle. This phenomenon shows that the annealing of a-LAGP/LATP

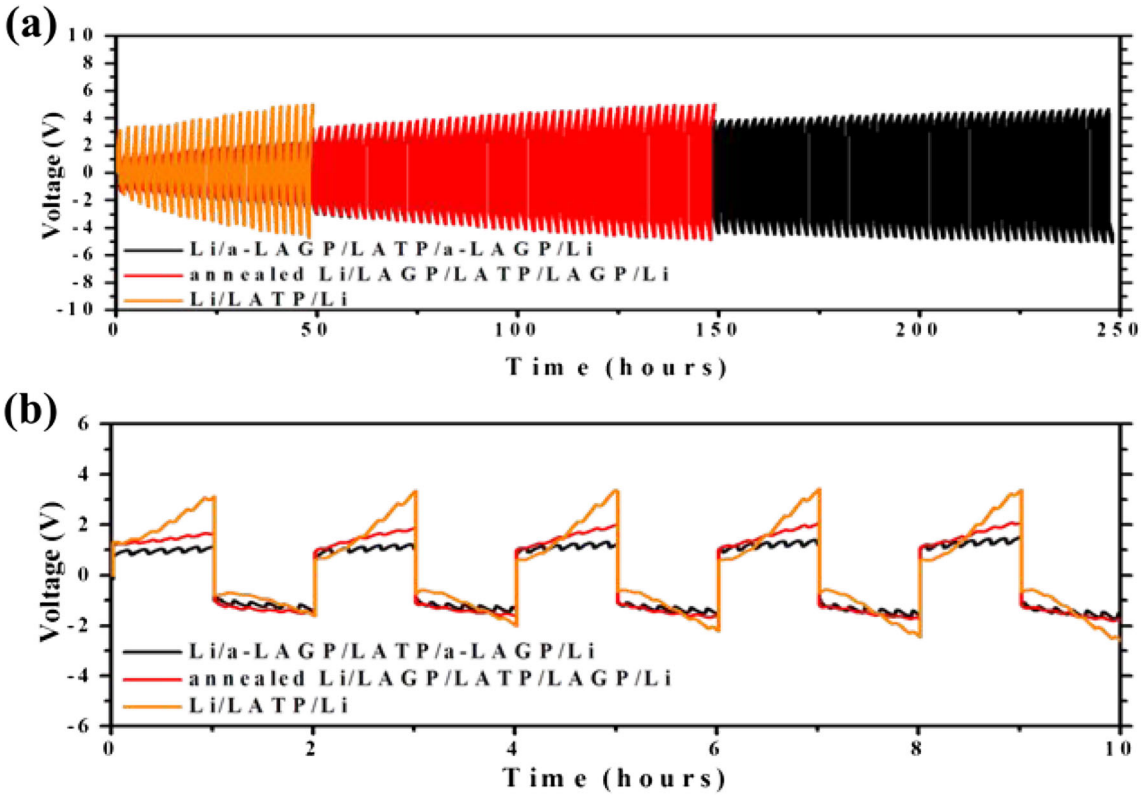

Fig. 4 **a** The galvanostatic cycle curve of Li/LATP/Li, Li/a-LAGP/LATP/a-LAGP/Li, and Li/LAGP/LATP/LAGP/Li symmetrical cells. **b** The curve after stretching the abscissa

and the galvanostatic cycling of Li/LATP/Li symmetrical cells have some similarity on the effect of LATP. We know that the contact and cycle of LATP with lithium metal will lead to the lithium intercalation of LATP [29], and eventually lead to the amorphization and even fragmentation of LATP. Similar Raman spectrum appears in the annealed LAGP/LATP indicates that in addition to the crystallization phenomenon, a-LAGP film has a complex reaction with LATP, which eventually leads to the degragation of the galvanostatic cycle stability of the Li/LAGP/LATP/LAGP/Li symmetrical cell.

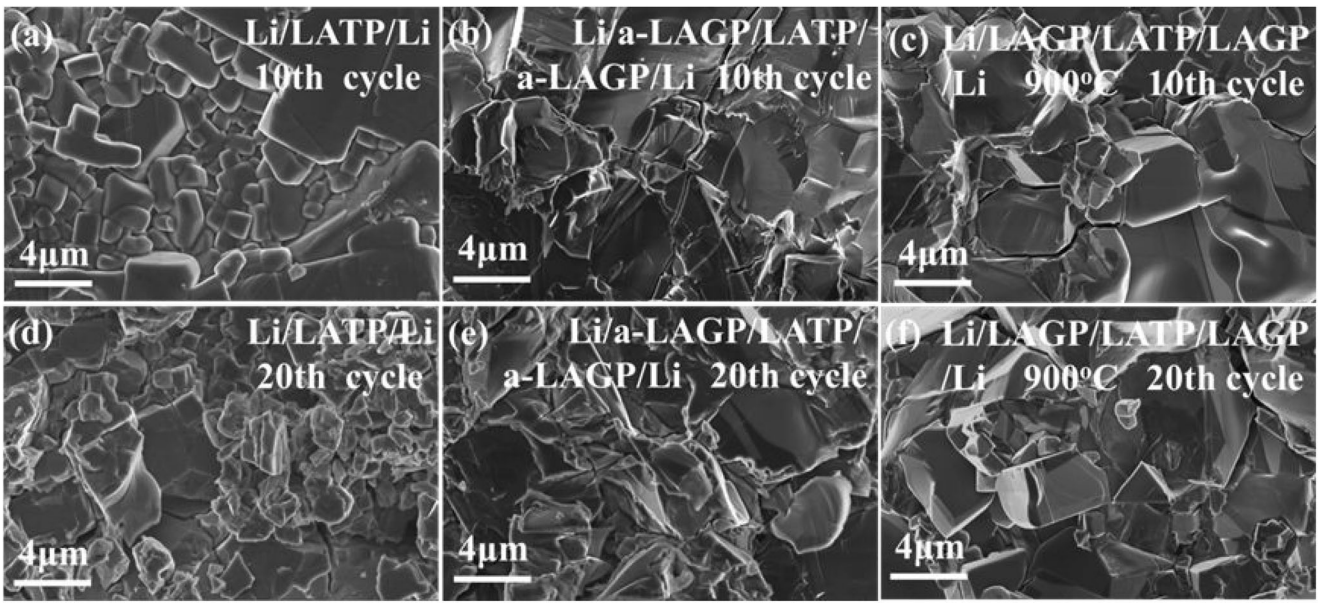

Fig. 5 Electrolytes morphology **a** and **d** of Li/LATP/Li, **b** and **e** of Li/a-LAGP/LATP/a-LAGP/Li, and **c** and **f** of Li/LAGP/LATP/LAGP/Li symmetrical cells after 10 cycles and 20 cycles

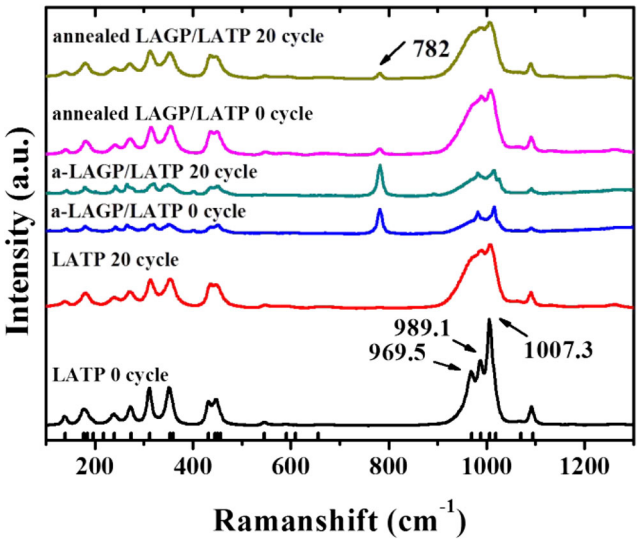

Fig. 6 Raman spectroscopy of LATP, a-LATP/LAGP, and annealed LAGP/LATP electrolytes with different cycles

In addition, polycrystalline ceramic materials have two kinds of lithium ion conduction mechanisms: grain boundary and grain, which lead to the uneven transport of lithium ion at the interface between ceramic materials and lithium anode [4, 30]. Compared with LAGP, the modification of a-LAGP obviously provides more uniform transport of lithium ions, leading to a better interface stability.

Conclusions

In summary, we have successfully improved the interface stability between LATP and lithium metal by a-LAGP. Li/a-LAGP/LATP/a-LAGP/Li symmetrical cell has better performance than Li/LATP/Li symmetrical cell. The mechanism is that Ge^{4+} in a-LAGP is more difficult to be reduced by lithium than Ti^{4+} in LATP, thus enabling stable chemical and crystalline structure properties. In addition, the amorphous nature of a-LAGP uniform the Li ion flux at the interface, which helps to suppress the formation of Li dendrite. LAGP and LATP have the same order of magnitude of ionic conductivity, which makes a-LAGP not have much effect on the overall conductivity. At the same time, due to the use of RF sputtering, the thickness of a-LAGP can be controlled to reduce its influence on the ionic conductivity. After annealing, Li/LAGP/LATP/LAGP/Li symmetrical cells do not exhibit better cycling characteristics. The reasons are as follows: The coating of a-LAGP on LATP is complete and continuous, and the annealed LATP appears uneven thickness. The amorphous layer is more uniform for the transport of ions, and there will be no electrolyte rupture due to the uneven transport of ions. In addition to crystallization, the complex reaction between a-LAGP and LATP results in the instability of the interface.

Funding information Financial support from the National Natural Science Foundation of China (Grants 61534005, 21761132030), General Armaments Department, People's Liberation Army of China (6140721040411), Natural Science Foundation of Jiangxi Province (20192ACBL20048), Scientific Research Project of Fujian Provincial Department of Education (JAT191150) are acknowledged.

References

1. Gao Z, Sun H, Fu L, Ye F, Zhang Y, Luo W (2018) Promises, challenges, and recent progress of inorganic solid-state electrolytes for all-solid-state lithium batteries. Adv Mater 30(17):1705702
2. West WC, Whitacre JF, Lim JR (2004) Chemical stability enhancement of lithium conducting solid electrolyte plates using sputtered LiPON thin films. J Power Sources 126:134–138
3. Cheng XB, Hou TZ, Zhang R, Peng HJ, Zhao CZ, Huang JQ (2016) Dendrite-free lithium deposition induced by uniformly distributed lithium ions for efficient lithium metal batteries. Adv Mater 28:2888–2895
4. Zhou W, Wang S, Li Y, Xin S, Manthiram A, Goodenough JB (2016) Plating a dendrite-free lithium anode with a polymer/ceramic/polymer sandwich electrolyte. J Am Chem Soc 138:9385–9388
5. Manthiram A, Yu X, Wang S (2017) Lithium battery chemistries enabled by solid-state electrolytes. Nat Rev Mater 2:16103
6. Xu XX, Wen ZY, Yang XL, Zhang JC, Gu ZH (2006) High lithium ion conductivity glass-ceramics in Li2O–Al2O3–TiO2–P2O5 from nanoscaled glassy powders by mechanical milling. Solid State Ionics 177:2611–2615
7. Xu X, Wen Z, Gu Z (2004) Lithium ion conductive glass ceramics in the system Li1.4Al0.4(Ge1−xTix)1.6(PO4)3 (x=0–1.0). Solid State Ionics Diff React 171:207–213
8. Ma C, Chen K, Liang CD, Nan CW, Ishikawa R, More K, Chi MF (2014) Atomic-scale origin of the large grain-boundary resistance in perovskite Li-ion-conducting solid electrolytes. Energy Environ Sci 7:1638
9. Kasper HM (1969) Series of rare earth garnets Ln3+3M2Li+3O12 (M=Te, W). Inorg Chem 8:1000–1002
10. Hayashi A, Minami K, Ujiie S, Tatsumisago M (2010) Preparation and ionic conductivity of Li7P3S11−z glass-ceramic electrolytes. J Non-Cryst Solids 356:2670–2673
11. Lim HD, Lim HK, Xing X, Lee BS, Liu H, Coaty C (2018) Solid electrolyte layers by solution deposition. Adv Mater Interfaces 5(8): 1701328
12. Lim HD, Yue X, Xing X, Petrova V, Gonzalez M, Liu H (2018) Designing solution chemistries for low-temperature synthesis of sulfide-based solid electrolytes. J Mater Chem A. https://doi.org/10.1039/C8TA01800F
13. Zhao EQ, Ma FR, Guo YD, Jin YC (2016) Stable LATP/LAGP double-layer solid electrolyte prepared via a simple dry-pressing method for solid state lithium ion batteries. RSC Adv 6:92579–92585
14. Zhu YZ, He XF, Mo YF (2015) Origin of outstanding stability in the lithium solid electrolyte materials: insights from thermodynamic analyses based on first-principles calculations. ACS Appl Mater Interfaces 7:23685–23693
15. Liu YL, Sun Q, Zhao Y, Wang BQ, Kaghazchi P, Adair KR, Li RY, Zhang C, Liu JR, Kuo LY, Hu YF, Sham TK, Zhang L, Ynag R, Lu SG, Song XP, Sun XL (2018) Stabilizing the interface of NASICON solid electrolyte against Li metal with atomic layer deposition. ACS Appl Mater Interfaces 10:31240–31248
16. Kotobuki M, Hoshina K, Kanamura K (2011) Electrochemical properties of thin TiO2 electrode on Li1+xAlxGe2−x(PO4)3 solid electrolyte. Solid State Ionics 198:22–25

17. Wolcott A, Smith WA, Kuykendall TR, Zhao YP, Zhang JZ (2099) Photoelectrochemical water splitting using dense and aligned TiO2 nanorod arrays. Small 5:104–111
18. Hoshina K, Yoshima K, Kotobuki M, Kanamura K (2012) Fabrication of LiNi0.5Mn1.5O4 thin film cathode by PVP sol–gel process and its application of all-solid-state lithium ion batteries using Li1+xAlxTi2−x(PO4)3 solid electrolyte. Solid State Ionics 209-210:30–35
19. Ling Q, Ye ZZ, Xu HR, Zhu GS, Zhang XY, Yu AB (2016) Preparation and electrical properties of amorphous Li-Al-Ti-P-O thin film electrolyte. Mater Lett 169:42–45
20. Chen KH, Wood KN, Kazyak E, Lepage WS, Davis AL, Sanchez AJ, Dasgupta NP (2017) Dead lithium: mass transport effects on voltage, capacity, and failure of lithium metal anodes. J Mater Chem A 5:11671–11681
21. Dashjav E, Ma QL, Xu Q, Tsai CL, Giarola M, Mariotto G, Tietz F (2018) The influence of water on the electrical conductivity of aluminum-substituted lithium titanium phosphates. Solid State Ionics 321:83–90
22. Lasri K, Dahbi M, Liivat A, Brandell D, Edstrom K, Saadoune I (2013) Intercalation and conversion reactions in Ni0.5TiOPO4 Li-ion battery anode materials. J Power Sources 229:265–271
23. Fu Y, Ming H, Zhao SY, Guo J, Chen MZ, Zhou Q, Zheng JW (2015) A new insight into the LiTiOPO4 as an anode material for lithium ion batteries. Electrochim Acta 185:211–217
24. Giarola M, Sanson A, Tietz F, Pristat S, Dashjay E, Rettenwander D, Redhammer GJ, Mariotto G (2017) Structure and vibrational dynamics of NASICON-type LiTi2(PO4)3. J Phys Chem C 121: 3697–3706
25. Beneventi P, Bersani D, Lottici PP, Kovacs L, Cordioli F, Montenero A, Gnappi G (1995) Raman study of Bi2O3-GeO2-SiO 2 glasses. J Non-Cryst Solids 192&193:258–262
26. Grzechnikyz A, Chizmeshyay AVG, Wolfy GH, McMillan PF (1998) J Phys Condens Matter 10:221–233
27. Verweij H, Buster JHJM (1979) The structure of lithium, sodium and potassium germanate glasses, studied by Raman scattering. J Non-Cryst Solids 34:81–99
28. Furukawa T, White WB (1991) Raman spectroscopic investigation of the structure of silicate glasses. IV Alkali–silico–germanate glasses. J Chem Phys 95:776–784
29. Wang X, Zeng W, Hong L, Xu WW, Yang HK, Wang F, Duan HG, Tang M, Jiang HQ (2018) Stress-driven lithium dendrite growth mechanism and dendrite mitigation by electroplating on soft substrates. Nat Energy 3:227–235
30. Cheng L, Chen W, Kunz M, Persson K, Tamura N, Chen GY, Doeff M (2015) Effect of surface microstructure on electrochemical performance of garnet solid electrolytes. ACS Appl Mater Interfaces 7:2073–2081